Voyager 2 UVS Observations of Jupiter During the Comet Shoemaker-Levy 9 Impact Events

R. J. Vervack, Jr.
J. Collins
J. B. Holberg
B. R. Sandel
F. Herbert
A. J. Dessler
W. T. Forrester
and
A. L. Broadfoot

Lunar and Planetary Laboratory
University of Arizona

Poster presented at the 26th Annual Meeting
of the Division for Planetary Sciences
Bethesda, Maryland, October 31–November 4, 1994

Description of the Observations

Voyager 2 Ultraviolet Spectrometer (UVS) observations of Jupiter began on July 8 and continued through August 15 with approximately 18 hours of real-time data collected each day. Data were collected for impacts A, B, C, D, F, G, H, L, Q1, Q2, R, T, U, V, and W, as well as during the predicted impact times for the "missing" fragments J and M. Data from impacts E, K, N, P1, P2, and S were not collected because they occurred during gaps in scheduled ground-station coverage. The time resolution of these observations is 3.84 seconds.

The geometry of the observations is illustrated in Figure 1. *Voyager 2* had a relatively direct view of the Jovian hemisphere where the impacts occurred; however, it was approximately 41 AU from Jupiter.

The *Voyager* UVS is an objective grating spectrometer covering the wavelength range of 500–1700 Å in 126 contiguous channels with a spectral resolution of approximately 18 Å for a point source. A detailed description of the instrument may be found in Broadfoot *et al.* (1977).

Statistical Analysis

A preliminary examination of the UVS data revealed no obvious signals which might correspond to impact phenomena. In order to investigate the possibility that more subtle impact-related events were present in the data and to establish a formal statistical upper limit for emissions from the impacts, we have evaluated the UVS data set as follows.

We selected a subset of data for statistical analysis covering the period from July 16 18:12:32 to July 22 12:59:53 (equivalent Earth-based UT observing time). Due to sporadic gaps in Deep Space Network tracking support of *Voyager 2*, data were not received for approximately 30 hours within this interval, corresponding to the impacts of fragments E, K, N, P1, P2 and S. A total of 102,573 spectra, each of 3.84 second duration, were received. Of these, 1943 spectra were excluded due to bit-level transmission errors. A total of 100,630 spectra, spanning more than 107 hours, were therefore used in this analysis.

We defined temporal windows in the data set corresponding to the impact times and their associated uncertainties as reported by Yeomans and Chodas (1994). We then searched these regions for spectra with anomalously high count rates, focusing our attention on the wavelength ranges 905–1115 Å and 1340–1670 Å. In both of these wavelength ranges, elevated count rates were found for several spectra within the specified temporal windows.

In order to determine the statistical significance of these events, we examined the observed frequency of integrated counts in these spectral bands, using as our statistical population only those spectra *outside* the temporal windows corresponding to the impact times. The resulting frequency distribution is presented in Figure 2 for the wavelength range 1340–1670 Å, while Figure 3 shows the distribution for the range 905–1115 Å. Figures 2 and 3 also show the locations of the two most significant spectra within the impact windows as listed in Tables 1 and 2, respectively.

The observed frequency distributions are not represented adequately by either normal or poisson distributions. In particular, the observed distributions have an exponential tail of high-count spectra. Consequently, we used the observed count distributions to empirically determine the probabilities of the spectra with the largest count rate for each impact occurring by chance. These cumulative distributions were calculated for the same statistical populations that are shown in Figures 2 and 3. For the 1340–1670 Å distribution, the mean and standard deviation are 10.34 counts and 7.09 counts, respectively. The mean and standard deviation for the 905–1115 Å distribution are 3.36 counts and 3.34 counts.

The slopes of the exponential tails differ in Figures 2 and 3, most likely due to the presence of a MgF_2 window which covers the long wavelength end of the detector. This wavelength region exhibits enhanced counting of background spectra compared to the uncovered region, indicating that the presence of the MgF_2 window could skew the distribution of counts toward larger values.

Table 1 summarizes the statistical significance of the largest single event observed in each of the impact windows in wavelength range 1340–1670 Å. The second column lists the integrated number of counts in the spectral bandpass for the spectrum having the highest count rate in each window, and the third column indicates the number of standard deviations corresponding to this count. The fourth column lists the probability that the spectrum would have occurred by chance *within that temporal window*. Event A, for example, is a 7.71-σ event (65 counts) which would occur by chance 0.38% of the time in any 48 spectra (3 minute interval). The fourth column specifies the duration of each window. Because no observations of fragment J and only one observation of fragment M were reported, a window of 10 minutes was arbitrarily chosen. Additionally, as no uncertainty value was available for fragment G2, we used the Yeomans and Chodas two-minute uncertainty for fragment G. The last column of Table 1 identifies the equivalent Earth-based observing time of the largest event in each of the windows.

The spectrum corresponding to event A has by far the largest number of counts. If we were to consider only the time period defined by the window for impact A, this high count rate would be statistically significant. If, however, we calculate the probability of observing this spectrum by chance during *all* of the temporal windows, we obtain a probability of 0.09, which is not significant. Thus, we conclude that no spectra occurring within our event windows exhibit excess count rates. In order to establish an upper limit for all of the events observed we adopt the conservative approach of using the spectrum listed in Table 1 for impact A as an operational upper limit.

Table 2 is the analog of Table 1 for the wavelength range 905–1115 Å. As in the long wavelength case, we adopt the conservative approach of using the spectrum listed in Table 2 for impact T as an operational upper limit.

Table 1. Results of the Statistical Analysis for 1340–1670 Å

Impact	Integrated Counts	Standard Deviation	Probability of Occurring Randomly	Time Window (minutes)	Corresponding Earth Observation Time (UT)
A	65	7.71	0.0038	3	JUL 16 20:11:12
B	27	2.35	0.221	6	JUL 17 2:50:27
C	36	3.62	0.260	4	JUL 17 7:12:58
D	34	3.34	0.262	3	JUL 17 11:53:38
F	45	4.89	0.113	5	JUL 18 0:34:25
G	27	2.35	0.364	2	JUL 18 7:32:09
G2	43	4.61	0.063	2	JUL 18 7:34:39
H	29	2.63	0.215	1	JUL 18 19:31:36
J	54	6.16	0.061	10	JUL 19 2:35:21
L	13	0.38	0.038	1	JUL 19 22:16:11
M	32	3.06	0.302	10	JUL 20 5:46:07
Q2	36	3.62	0.323	6	JUL 20 19:46:51
Q1	59	6.87	0.013	4	JUL 20 20:13:28
R	35	3.48	0.239	3	JUL 21 5:32:55
T	41	4.33	0.228	7	JUL 21 18:09:56
U	36	3.62	0.342	7	JUL 21 21:56:49
V	25	2.07	0.168	5	JUL 22 4:23:16
W	28	2.49	0.372	3	JUL 22 8:06:18

Table 2. Results of the Statistical Analysis for 905–1115 Å

Impact	Integrated Counts	Standard Deviation	Probability of Occurring Randomly	Time Window (minutes)	Corresponding Earth Observation Time (UT)
A	11	2.28	0.357	3	JUL 16 20:12:44
B	12	2.58	0.285	6	JUL 17 2:48:08
C	19	4.68	0.149	4	JUL 17 7:12:35
D	8	1.39	0.087	3	JUL 17 11:54:20
F	20	4.97	0.139	5	JUL 18 0:35:34
G	7	1.09	0.104	2	JUL 18 7:32:21
G2	10	1.98	0.365	2	JUL 18 7:34:08
H	8	1.39	0.371	1	JUL 18 19:31:59
J	26	6.77	0.050	10	JUL 19 2:43:17
L	13	2.88	0.184	1	JUL 19 22:16:23
M	15	3.48	0.359	10	JUL 20 5:48:18
Q2	15	3.48	0.356	6	JUL 20 19:44:55
Q1	9	1.69	0.102	4	JUL 20 20:11:10
R	14	3.18	0.308	3	JUL 21 5:32:48
T	27	7.07	0.032	7	JUL 21 18:08:43
U	20	4.97	0.182	7	JUL 21 21:52:20
V	17	4.08	0.250	5	JUL 22 4:21:24
W	21	5.27	0.067	3	JUL 22 8:04:15

Flux Calculations

Because *Voyager 2* detected no statistically significant signal, we can only quote upper limits on the radiated power escaping the Jovian atmosphere. Table 3 lists the upper limits on the radiated power integrated over the specified wavelength ranges. We do not quote an upper limit for the wavelength range from 500–900 Å because we do not expect a significant amount of radiation to escape the Jovian atmosphere at these wavelengths due to absorption by H_2.

Table 3. Upper Limits on the Radiated Power

Wavelength Range	Radiated Power $\left(\frac{\text{ergs}}{\text{sec}}\right)$	Radiated Power $\left(\frac{\text{photons}}{\text{sec}}\right)$
1340–1670 Å	1.9×10^{24}	1.5×10^{35}
905–1115 Å	5.6×10^{22}	2.9×10^{33}

We can carry the analysis further by accounting for the effects of atmospheric absorption. To do this, we assume that the integrated power is spread uniformly over the wavelength range and assume that the source is at a specific level in the atmosphere. We compute the wavelength-dependent absorption of the overlying atmosphere, and hence the spectrum of the emerging radiation. The power distribution can then be integrated over the wavelength range once more and associated with an area for the emitting region to yield an integrated flux. To estimate the amount of absorption, we have used the model atmosphere based upon the analysis of the *Voyager 2* UVS stellar occultation by Festou *et al.* (1981).

The results of this procedure are shown in Figure 4 for the wavelength range 1340–1670 Å. This figure relates the integrated flux over the wavelength range to the area of the emitting region. Over 1340–1670 Å, we need consider only continuum absorption by hydrocarbons. We have included absorption by CH_4, C_2H_2, and C_2H_6, the only hydrocarbons of significance according to Festou *et al.* (1981). We do not consider Rayleigh scattering since it is not significant even at 500 μbar, the lowest level we consider.

The three curves in Figure 4 represent three different levels for the fireball. The integrated power at each level is obtained by multiplying the flux by the corresponding area (in cm). This power is a constant along each of the three curves. Below the 500 μbar level, the hydrocarbon column densities are too large for significant amounts of radiation to escape unless the initial radiation involves fluxes or areas we consider unreasonably large, and we chose this level as our cut-off.

In Figure 5, we have carried the analysis one step further. Here, we have assumed that the fireball radiates as a blackbody and show the relationship between the area of the emitting region and the corresponding blackbody temperature. This relationship was derived by assuming a temperature for the blackbody, calculating radiated fluxes over our wavelength range, propagating these fluxes through the atmosphere, integrating the resulting fluxes to yield an integrated escaping flux, and solving for the area that yields the upper limit to the escaping power. We have done this for the same three starting levels as in Figure 4.

The circle in Figure 5 corresponds to the 8000 K, 10-km diameter fireball observed for impact G by the *Galileo* instruments (P. Weissman, personal communication, 1994). To fall on our "no absorption" curve, the fireball would need a diameter of roughly 30 km and a temperature of 15,000 K. This indicates that our observed upper limit on the power may be somewhat higher than the true power level. The required increase in temperature is explained by the fact that only the tail of an 8000 K blackbody energy distribution falls within our passband. However, we related our upper limit to blackbody radiation only to provide a physical basis for interpretation. It is entirely possible that the fireballs do not radiate as blackbodies, and we believe that an upper limit on the power in our wavelength range is therefore a valid quantity.

Acknowledgements

This work was supported by NASA Grant NAGW-3657.

References

Broadfoot, A. L., B. R. Sandel, D. E. Shemansky, S. K. Atreya, T. M. Donahue, H. W. Moos, J. L. Bertaux, J. E. Blamont, J. M. Ajello, D. F. Strobel, J. C. McConnell, A. Dalgarno, R. Goody, M. B. McElroy, and Y. L. Yung, Ultraviolet spectrometer experiment for the *Voyager* mission, *Space Sci. Rev.* **21**, 183–205, 1977.

Festou, M. C., S. K. Atreya, T. M. Donahue, B. R. Sandel, D. E. Shemansky, and A. L. Broadfoot, Composition and thermal profiles of the Jovian upper atmosphere determined by the *Voyager* ultraviolet stellar occultation experiment, *J. Geophys. Res.* **86**, 5715–5725, 1981.

Yeomans, D. K., and P. W. Chodas, *Jet Propulsion Laboratory Interoffice Memorandum* **314.10-87**, 1994.

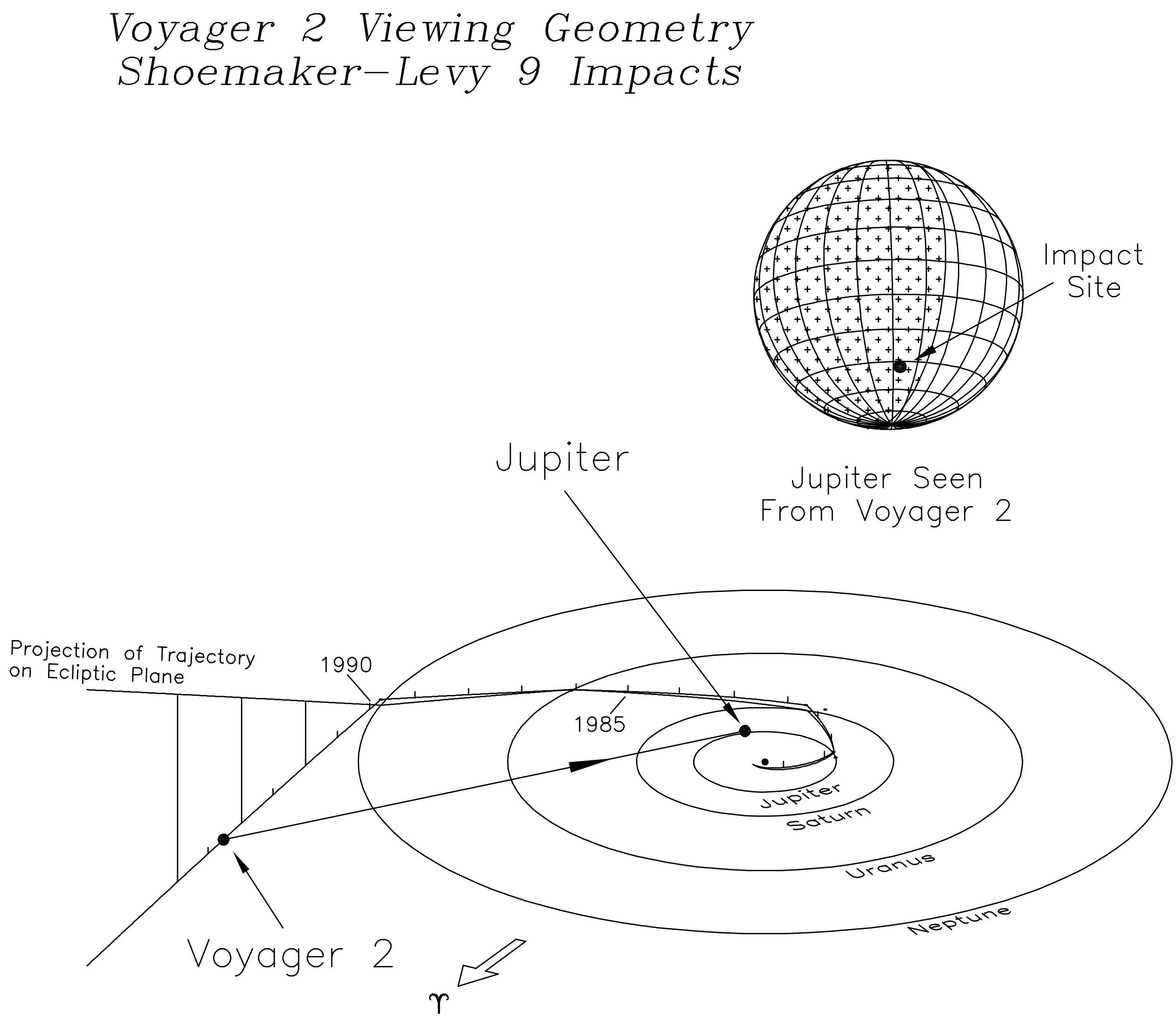

Figure 1. Illustration of the *Voyager 2* UVS observing geometry. During its August 1989 encounter with Neptune, *Voyager 2* flew over Neptune's northern pole and assumed a trajectory that has since carried it well south of the ecliptic plane. As can be seen in the close-up of Jupiter, this trajectory has fortuitously resulted in *Voyager 2* having a relatively direct view of the Shoemaker-Levy 9 impact sites.

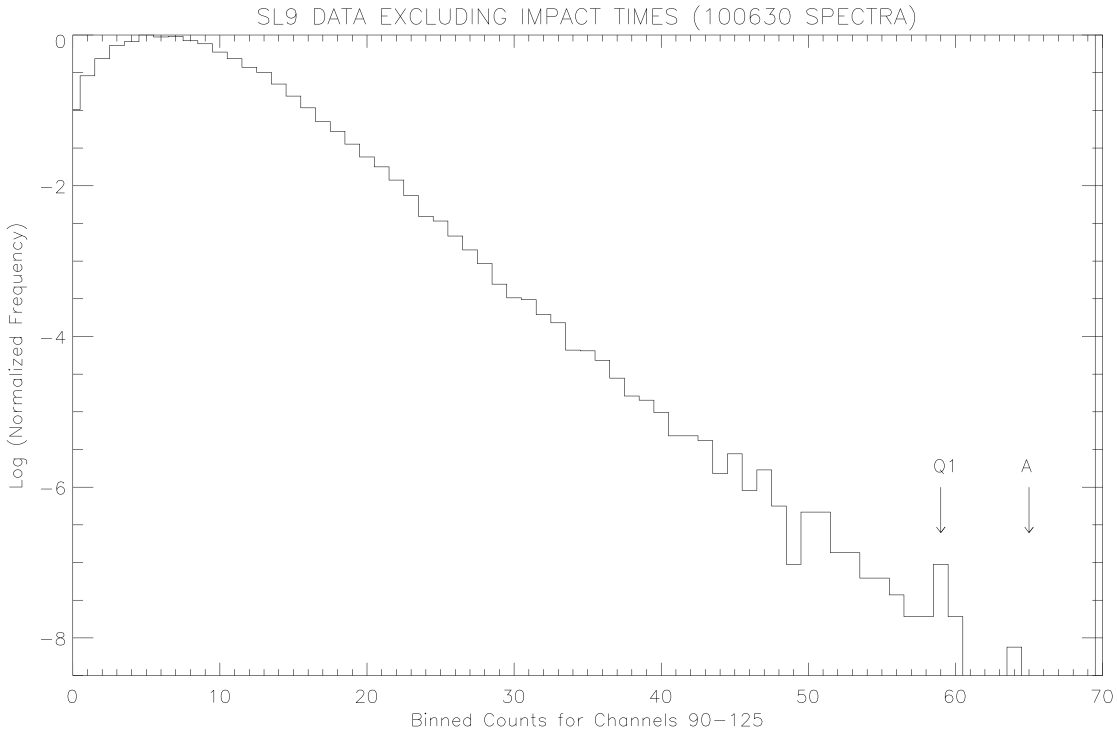

Figure 2. Normalized frequency distribution for the wavelength range 1340–1670 Å. The arrows indicate the locations of the two spectra with the highest count rates in the temporal windows examined for each impact. These spectra correspond to the Q1 and A impacts listed in Table 1.

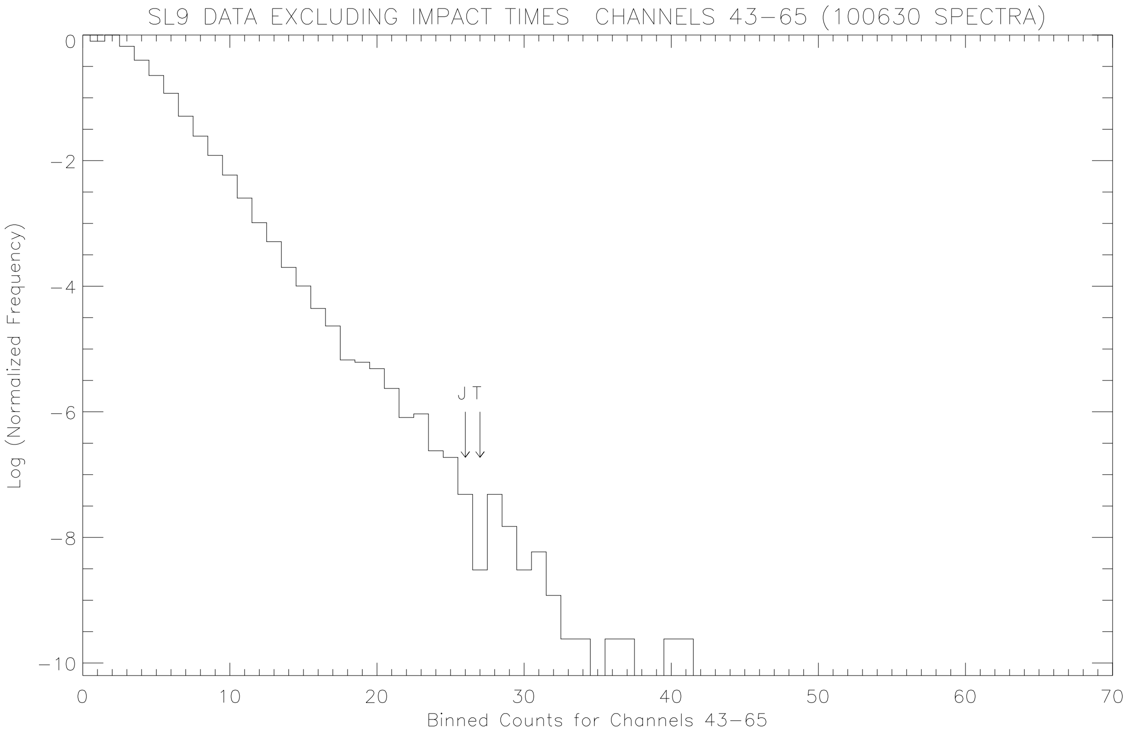

Figure 3. Normalized frequency distribution for the wavelength range 905–1115 Å. The arrows indicate the locations of the two spectra with the highest count rates in the temporal windows examined for each impact. These spectra correspond to the J and T impacts listed in Table 2.

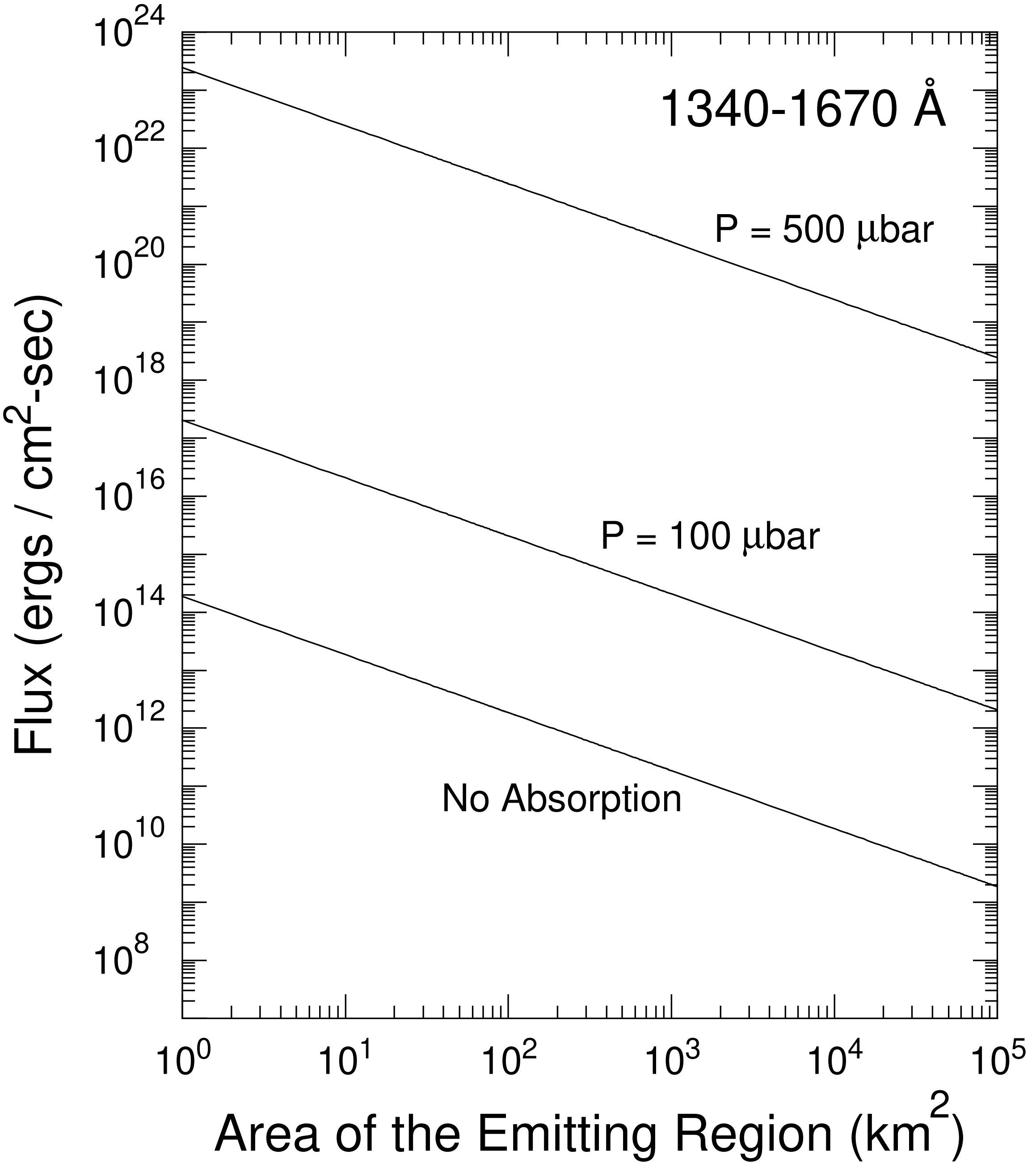

Figure 4. Relationship between the radiated flux and the area of the emitting region that yields the upper limit on the power integrated over the wavelength range 1340–1670 Å set by the *Voyager 2* UVS observations. The three curves correspond to sources at different levels in the Jovian atmosphere. The "no absorption" curve pertains to a source just outside the atmosphere.

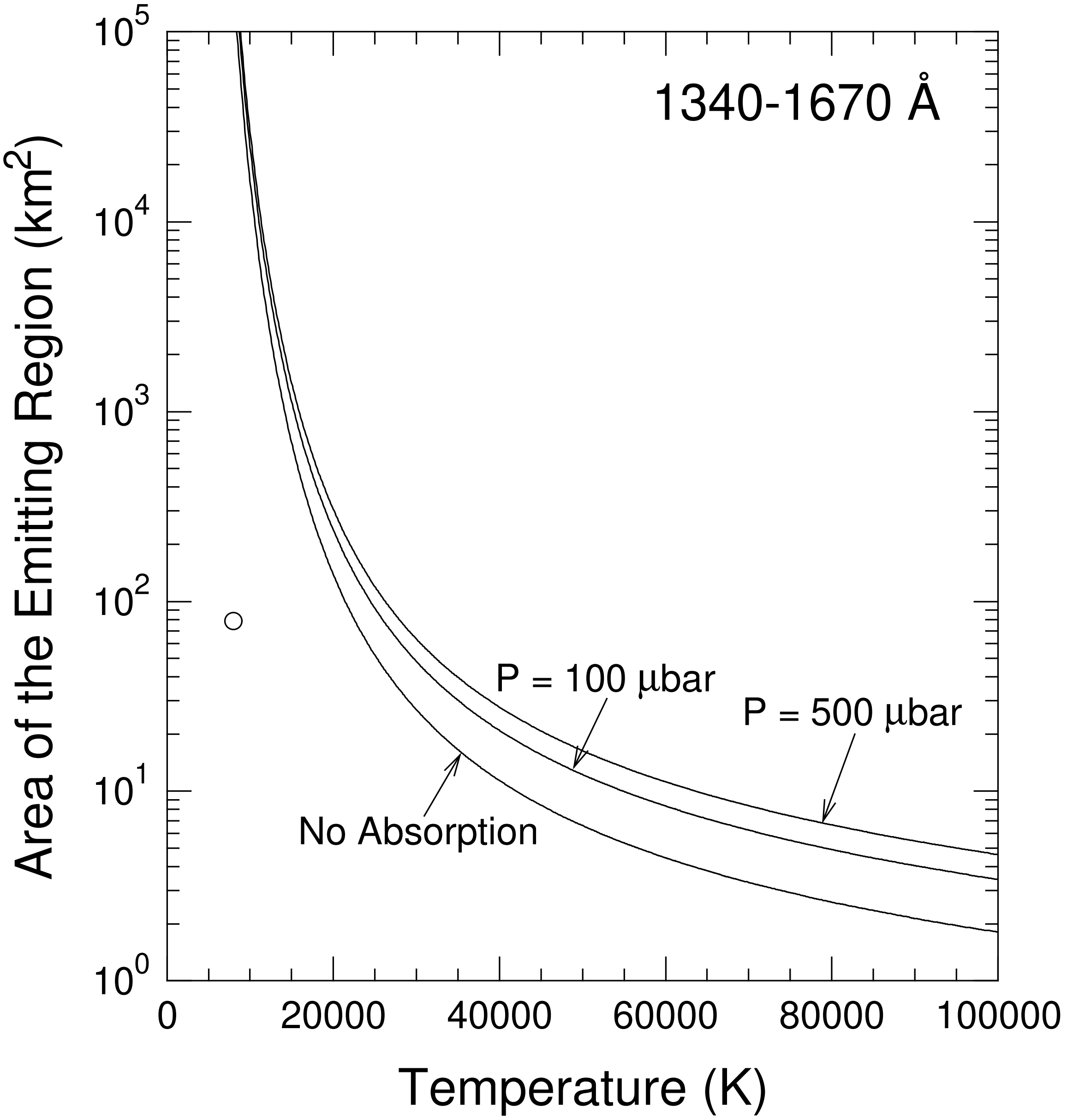

Figure 5. Relationship between the area of the emitting region and the blackbody temperature that yields the upper limit on the power integrated over the wavelength range 1340–1670 Å set by the *Voyager 2* UVS observations. The three curves correspond to sources at different levels in the Jovian atmosphere. The "no absorption" curve pertains to a source just outside the atmosphere. The circle corresponds to the 8000 K, 10-km diameter fireball observed by the *Galileo* instruments for impact G (P. Weissman, personal communication, 1994).